

Effect of Mg-doping on the degradation of LiNiO₂-based cathode materials by
combined spectroscopic methods

Shunsuke Muto¹, Kazuyoshi Tatsumi¹, Yuji Kojima¹, Hideaki Oka², Hiroki Kondo²,
Kayo Horibuchi² and Yoshio Ukyo²

¹Graduate School of Engineering, Nagoya University, Chikusa-ku, Nagoya, Aichi
464-8603, Japan

²Toyota Central R&D Laboratories Inc., Nagakute, Aichi 480-1192, Japan

Abstract

The performance of a LiNiO₂-based cell has been shown to be significantly improved by Mg-doping of LiNi_{0.8}Co_{0.15}Al_{0.05}O₂ cathode materials. Here, the effects of Mg-doping were examined by electrochemical impedance spectroscopy (EIS) and scanning transmission electron microscopy-electron energy loss spectroscopy (STEM-EELS). Spatial mapping of the product phases in the Mg-doped sample showed less degradation after charge-discharge cycling tests at 70 °C compared with undoped samples. In addition, degraded regions observed near the surface of primary active material particles were identified as an intermediate phase, containing tetrahedrally coordinated Ni, in contrast to the NiO-like phase found in undoped samples. These microstructural observations are consistent with electrochemical measurements.

1. Introduction

Cathode materials are key components in rechargeable lithium-ion batteries, and have been intensively studied since the advent of high-energy-density LiMO_2 (M= Co, Ni) cathodes in 1980¹, and the subsequent commercial success of LiCoO_2 cathode materials. Although LiCoO_2 is considered to be a well-established material in mobile applications, alternatives have become necessary because of the high cost and toxicity of LiCoO_2 in high-power and large-scale energy-storage applications. LiNiO_2 ²⁻⁶ was a promising alternative, stimulating extensive studies on cationic substitution for Ni, in an attempt to stabilize the layered structure of the material, including Co⁷⁻⁹, Fe¹⁰, Mn¹¹⁻¹³, Al^{14, 15}, Mg¹⁶⁻¹⁸, Co/Al¹⁹⁻²², and Co/Mg^{23, 24}. Of this wide range of materials, $\text{LiNi}_{1-x-y}\text{Co}_x\text{Al}_y\text{O}_2$ (NCA), in which the stability is improved by Al doping, was the most successful alternative to LiCoO_2 because of the higher reversible capacity and better environmental compatibility. However, in automotive applications, degradation at elevated temperature (60-80 °C) was found to be a serious problem⁶⁻¹⁵, due to, for example, capacity fading and impedance rise²⁵⁻²⁸. Capacity fading of the NCA battery was mainly attributed to the cathode material²⁹, although no appreciable changes could be detected by macroscopic analysis techniques such as X-ray diffraction (XRD).

To provide more insight into the degradation processes in NCA batteries at elevated temperature, we applied a statistical signal processing technique to spectrum imaging (SI) datasets obtained by scanning transmission electron microscopy (STEM) and electron energy-loss spectroscopy (EELS), to resolve the overlapping spectral components, thereby visualizing the spatial distribution of each different chemical state on a relative concentration map³⁰⁻³². This method successfully revealed that a NiO-like phase was distributed near the surface of NCA particles after the charge-discharge

cycling test at elevated temperature, and that device degradation could be largely explained by the evolution of this NiO-like phase, particularly near the NCA particle surface^{31, 33}. In our series of studies the ‘NiO-like’ phase refers to the local atomic configuration and chemical states probed by EELS rather than to a long-range order having translational symmetry.

To improve device stability, we proposed Mg-doped-NCA ($\text{LiNi}_{0.75}\text{Co}_{0.15}\text{Al}_{0.05}\text{Mg}_{0.05}\text{O}_2$) as a cathode material³⁴. This actually suppressed capacity fading and resistance increase during cycling at 60 °C. We examined the state of Mg in $\text{LiNi}_{0.75}\text{Co}_{0.15}\text{Al}_{0.05}\text{Mg}_{0.05}\text{O}_2$ by neutron diffraction³⁴, EELS, XAFS, and first-principles theoretical calculations³⁵, and found that Mg is mainly substituted at the Ni site, and that Ni-O bonding around the dopant was significantly increased due to a greater degree of ionic bonding.

Here, we examine how Mg-doping exerts influence on the local spatial and electronic structure of NCA cathodes in cycling tests at 70 °C, using electrochemical impedance spectroscopy (EIS), STEM-EELS, and SI multivariate curve resolution (MCR) techniques, in comparison between the above microscopic and macroscopic electrochemical measurements.

2. Experimental

2.1 Cell fabrication and test conditions

Cathode materials, $\text{LiNi}_{0.8-x}\text{Co}_{0.15}\text{Al}_{0.05}\text{Mg}_x\text{O}_2$ ($x = 0, 0.05$), were prepared by a co-precipitation method. The undoped ($x = 0$) and Mg-doped ($x = 0.05$) materials are herein written as NCA and Mg-doped NCA, respectively. The size of the primary particles ranges between 100 nm and 1 μm , agglomerated to form secondary particles of $\sim 12 \mu\text{m}$ and

~7 μm on average for NCA and Mg-doped NCA, respectively.

Cell performance was examined using 18650-type (750 mAh) cylindrical cells with graphite as the anode material. The detailed cell fabrication procedure is described elsewhere³⁴. The positive and negative electrodes were wound with a polyethylene separator and then put into a cylindrical cell-case with 1M LiPF_6 dissolved in an ethylene carbonate/dimethyl carbonate/ethyl methyl carbonate (EC/DMC/EMC) mixed solvent (3:4:3 in volume). After several initial charge-discharge conditioning cycles, the high-temperature cycling test was carried out at a 2 C-rate for 500 cycles, in the voltage range 3.0 to 4.1 V, at 70°C. Reversible cell capacity was measured by charging the cells under constant voltage to 4.1 V and discharging it at a 0.1 C rate to 3.0 V at 20°C before and after cycling test. I-V resistance was obtained from voltage response in relation to the direct current for 10 s at 20°C³⁴.

After discharging to 3.0 V, the cell was disassembled in an Ar-filled glove box with great care to prevent a short circuit. A cell subjected only to the initial conditioning cycles was also disassembled in the same manner for comparison. Cathode samples were rinsed with DMC three times to completely remove residual electrolyte.

EIS was carried out using a three-electrode cell, with a Solartron 1255WB frequency response analyzer. The amplitude was 5 mV in the frequency range 0.01 Hz-100 kHz.

2.2 STEM-EELS Spectrum imaging and analysis

A focused ion beam thinning technique was used to produce 100 nm-thick samples with an area of ~10 μm^2 ; equivalent to secondary particle size in the cathode. STEM-EELS SI data were acquired at room temperature, using a Jeol JEM2100 S/TEM

for the low-loss region (including Li-K, Co- and Ni-M_{2,3} absorption edges), and a JEM2100F S/TEM with the spherical aberration of the illumination system corrected for the high-energy region (including O-K, Co- and Ni-L_{2,3} edges), both equipped with a Gatan Enfina 1000 spectrometer, in the same manner as previous studies. Data pre-processing and MCR analysis procedures were also the same as previously reported.

2.3 Theoretical O-K ELNES calculations

We calculated the theoretical electron energy-loss near edge structure (ELNES) of the transition from the O 1s to O 2p unoccupied states, using the augmented plane wave plus local orbital (APW+lo) band method, within the generalized gradient approximation (GGA; WIEN2k simulation package)³⁶, to compare the relative peak intensities and positions of experimental and theoretical spectra. For Ni *d* states, we adopted a Hubbard-type orbital-dependent interaction, in a similar manner to Ref.^{32, 35}. Supercells containing 56 to 128 atoms were used, with a core-hole explicitly introduced at the excited atom. Prior to spectral calculations, structural parameters were optimized using the projected augmented wave method (VASP simulation package)³⁷. For optimization, the Hubbard parameter, U_{eff} , was set to 6.7 eV (GGA+ U), which was obtained for LiNiO₂ by a self-consistent linear-response procedure³⁸. The atom positions were freely relaxed under the constraint of the given symmetry of the supercell, within the fixed supercell size, until the residual forces were reduced to less than 0.05 eV/Å. The final ELNES spectrum was broadened by a Gaussian function with a full width at half-maximum of 1.5 eV. In the spectral calculations, U_{eff} was set to 2.0 eV, because the peak energy positions in the O-K ELNES of NiO calculated using this value were most consistent with the experimental ones, as previously reported³⁹.

3. Results and Discussion

3.1 Cell performance

The effect of Mg-doping on the cycling durability at 70 °C showed the same trend as that at 60 °C³⁴, as shown in Fig. 1, and the low-rate capacity and I-V resistance of the cells before and after the cycling test were summarized in Table 1. The cyclability of the cell was improved by Mg-doping, although the initial cell capacity of the Mg-doped NCA was smaller than that of the undoped NCA. Conversely, the I-V resistance of the NCA cell increased by 53.9% after cycling, while Mg-doping suppresses the increase in cell resistance to just 29.2%. As mentioned in our previous study³⁴, the increase in resistance of the NCA cell can be attributed to the increasing impedance of the cathode. Therefore, the suppression of the resistance increase in the Mg-doped NCA can mainly be attributed to the cathode.

3.2 EIS measurements

EIS data were obtained using a three-electrode cell, with Li metal counter and reference electrodes, and with the potential set at 3.78 V vs. Li⁺/Li, which corresponds to 50% state of charge (SOC). Nyquist plots of both the NCA and Mg-doped NCA are shown in Fig. 2 (a) and (b), respectively. All Nyquist plots show two successive convex arcs, each corresponding to the high (left arc) and low (right arc) frequency ranges, respectively. The right arc in the low frequency range (~1 Hz) corresponds to the charge-transfer resistance of the cathode, since the diameter of the right arc showed clear correlation with electrode potential. In contrast, the diameter of the high frequency part (left arc) was independent of the cathode potential, as examined in the previous

paper²⁹. We presume that the left arc could comprise multiple effects such as the resistances of the lithium counter electrode and solid-electrolyte interphase (SEI) of cathode. Therefore, we herein focus on only the right arc. As can be clearly seen in Figs. 2(a) and (b), the impedance of the NCA cathode increased by a factor of 4.5 after cycling at 70 °C, whereas the impedance of the Mg-doped NCA cathode increased by only 10%.

We constructed an equivalent circuit (Fig. 2(c)) to evaluate the charge-transfer resistance (R_{ct}) of the cathodes. The equivalent circuit comprises the ohmic resistance (R_{sol}) and two RC-parallel circuits, each corresponding to the two successive arcs observed in Figs. 1(a) and (b). One of the RC circuits (corresponding to the cathode) includes the Warburg diffusion impedance (Z_w)⁴⁰.

Figures 3(a) and (b) show the temperature dependence of the reciprocal of the charge-transfer resistance ($1/R_{ct}$) for the two samples, obtained by the equivalent circuit analysis⁴⁰. The activation energies, evaluated from the slopes of the Arrhenius plots, were 61.7 and 66.4 kJ/mol for the fresh NCA and Mg-doped NCA cathodes, respectively. The activation energies of the charge-transfer resistance of Li-intercalation/deintercalation for LiCoO₂ thin film electrodes have been reported to be 60 and 61 kJ/mol, respectively⁴¹. In that work, it was concluded that desolvation of Li-ions during the charge-transfer reaction was responsible for such relatively large activation energies⁴¹. The activation energy of the lithium-ion transfer reaction through the graphite/electrolyte interface was also evaluated to be 53–60 kJ/mol, and it was concluded that the rate-determining step of the charge-transfer reaction of graphite was also desolvation⁴²⁻⁴⁴. The present activation energies for the charge-transfer reaction obtained for the LiNiO₂-based materials (61.7–66.4 kJ/mol) are larger than the reported

values by a factor of ~10%, though the activation energy depends on the composition of the electrolyte solution and on the composition of the active materials^{29,44,45}. We thus consider that the rate-determining step for the charge-transfer of NCA and Mg-NCA cathodes is also desolvation of Li-ions from the solvent, as in the above case.

Figure 3(a) shows that the activation energy for the charge-transfer of the NCA cathode increased by only 6% after cycling, whereas the geometry factor (the intercept of the straight line, extrapolated to infinite temperature) significantly decreased. This result indicates that the rise in impedance of the NCA cathode was caused by a reduction in the number of active site of the charge-transfer process. This is consistent with our previous reports, because the NiO-like degraded phase (with a nickel valence of +2) increased near the surface of the NCA particles during the cycling test^{29,31}, and is considered to be inactive towards the charge-transfer reaction. The frequency factor of the charge-transfer reaction of the NCA cathode was thus decreased by charge-discharge cycling.

In contrast, the Arrhenius plot of the charge-transfer resistance for Mg-doped NCA did not vary appreciably with cycling, as shown in Fig. 3(b), implying a different evolution of the microstructure associated with cycling in this case.

3.3 STEM-EELS SI-MCR

Typical examples of SI-MCR results for the samples after initial conditioning, and after 500 cycles at 70 °C, are shown in Fig. 4. Three spectral components are assumed, as in the case of our previous report³¹. Both types of sample were found to have resolved components in common. The first and third components are assigned to the original phase, and the lithium deficient phase, respectively³¹, while the second

component, distributed mainly near the surfaces and grain boundaries of the active material particles, is likely to differ from the original structural phase. Several conclusions can be drawn from these findings. Firstly, the O K ELNES pre-peak position of component 2 is different from that of the NiO-like phase previously observed³¹ (Fig. 4(a)). Secondly, in accordance with this, the Ni L_{2,3} ELNES of component 2 is also different from the NiO-like phase, displaying intermediate valency between the divalent and trivalent states (Fig. 4(a)). Thirdly, the relative concentration of component 2 is not significantly increased after 500 cycles at 70 °C. Finally, the average primary particle size in the cycled sample is smaller than that of the initially conditioned sample.

It is noted that the residual signal after cycling has a weak heterogeneous structure, rather than random statistical noise, suggesting that another underlying component could be extracted from the data, because of the uniqueness of the MCR solutions³². We thus attempted to apply 4-component MCR to the SI dataset of the sample (Fig. 5). The O K ELNES of the fourth component exhibits features similar to those of the NiO-like phase, and the 2D residuals (not shown) show no appreciable structure, although this component contains some Co, and the relative intensity of Ni-L_{2,3} is small. It is thus reasonable to conclude that this fourth component is due to the damaged surface layer produced during the FIB thinning process³³.

As in our previous work³³ on undoped NCA cathodes, degradation correlated with capacity fade and resistance increase with cycling can be investigated by measurement of the average radii of the particles (assuming spherical particle shape). The results are summarized in Table 2. No significant increase in the fraction of the product phase was observed after cycling, whereas considerable degradation is caused by cycling in

undoped samples, as reported in ref. 33. This result is consistent with the results in Section 3.1.

The NiO-like product phase in the undoped NCA samples has been correlated with fluorine distribution³¹, and therefore energy-filtered images using F K ELNES were examined (Fig. 6). Some F was distributed near the surface of the particles, but less than in the undoped samples. The low-loss region including Li K ELNES was also examined in the same manner as in our previous paper³². The MCR method yielded a much less surface-localized phase in comparison with previous reports, and its spectral profile was too unstable for repeated MCR applications to identify its chemical state. This result corresponds to less fluorine and lithium fluorides in the surface region of Mg-doped samples, suggesting that the Mg-doped cathode has increased stability against surface reactions with fluorine in the electrolyte.

Phosphorous was also found near the surface regions, though there observed no evolution of the phosphorous distribution by cycling, as also in the case of the undoped NCA³².

3.4 Theoretical ELNES of O K

Experimental O K and Ni L_{2,3} ELNESs of the initial LiNiO₂ phase, the NiO-like phase, and the new phase in the Mg-doped NCA sample (component 2 in Fig. 4(a)) are compared in Fig. 7 and Fig. 8(a), respectively. As mentioned in the previous section, the pre-peak position of O K ELNES for the Mg-doped sample is located between LiNiO₂ and NiO. In addition, the Ni L_{2,3} ELNES spectrum of the Mg-doped NCA sample appears to be a summation of the LiNiO₂ and NiO spectra. It is thus reasonable to assume that the new phase in Mg-doped NCA is an intermediate phase between the

LiNiO₂ and NiO-like local atomic configurations, probed by EELS, rather than a long-range order structure having translational symmetry. A candidate that exhibits the red-shift of the oxygen pre-peak could be an under-coordinated transition metal site, such as the tetrahedral site in the spinel structure. A nominal spinel-like composition, Li_{0.5}NiO₂, can be locally formed by Li and Ni ions settling on the tetrahedral site (from their original octahedral site) during degradation to the NiO-like phase³³, imposing an intermediate metastable state on the Ni ions. Indeed, the spinel phase has been experimentally observed in a LiCoO₂ cathode with a degraded surface⁴⁶.

It was difficult to fully reproduce the energy and intensity of the first peak of the LiNiO₂ phase, in contrast with the excellent agreement between experimental and theoretical O K ELNES for NiO, as shown in Fig. 7(b). This may be attributed to limited many-body interactions of the O 2p and Ni 3d electrons in these GGA+*U* calculations. Varying the *U*_{eff} value did not improve the result. Moreover, the experimental energy between the first peak and the threshold of the main structure at 535 eV (Fig. 6) is approximately 6 eV, which is larger than the GGA+*U* band gap of 5 eV. The theoretical underestimate of the band gap could be closely related to the incorrect first peak position. To our knowledge, no successful theoretical reproduction of the O-K spectrum of LiNiO₂ has been reported. Further theoretical considerations with higher accuracy than GGA+*U* will be left to a future study.

To reproduce the local chemical environment around oxygen in the new phase, the virtual Ni₃O₄ spinel structure was assumed instead of Li_{0.5}NiO₂ to simplify the calculation procedure, since ELNES is mainly affected by first nearest-neighbor coordinated atoms. The O K ELNES for this structure was calculated according to the same scheme as the NiO phase, as shown in Fig. 8(b). The energy axis was calibrated by

the position of the highest peak at around 542 eV. The theoretical O K ELNES for NiO has already been reported to be in good agreement with experiment³⁹. In the intermediate spinel phase, Ni occupies both the tetrahedral and octahedral sites, the different crystal fields of which are reflected in the first O K ELNES peak, because the oxygen 2p bands are hybridized with the Ni 3d bands. As expected, the first Ni₃O₄ peak (O 2p hybridized with Ni 3d at the tetrahedral site) was at a lower energy than the second peak (O 2p hybridized with Ni 3d at the octahedral site). The relative energy of the first peak was roughly consistent with the experimental spectrum of the intermediate phase, as in the case of NiO. In this case, the Ni L_{2,3} ELNES should exhibit an intermediate spectral profile between the trivalent and divalent states, which is consistent with the experimental result.

4. Conclusions

The degradation of Mg-doped NCA cathode materials by cycling at elevated temperature was examined by EIS and STEM-EELS SI techniques. The obtained results are summarized as follows. (1) The capacity fade and internal resistance rise associated with charge-discharge cycling at 70 °C were significantly suppressed in the Mg-doped NCA cathode. (2) The EIS results suggested that the impedance rise in the cycled NCA cathode was caused by the reduction in the number of active site for the charge transfer process, which is attributable to the formation of the surface degradation phase, as reported in our previous work. Conversely, the Mg-doped NCA cathode exhibited little change in either activation energy or frequency factor. (3) Spatial mapping of the Mg-doped NCA sample showed much less degradation than the NCA cathode, after cycling at 70 °C. The degraded regions of the Mg-doped NCA cathode are suggested to

be in an intermediate spinel-like phase, rather than the NiO-like phase seen in undoped NCA. This spinel-like phase did not increase under cycling, resulting in reduced capacity fade and impedance rise.

Acknowledgments

This work is supported in part by a Grant-in-Aid for Scientific Research (KAKENHI) in Priority Area (#474) “Atomic Scale Modification” from MEXT, Japan.

References

1. K. Mizushima, P. C. Jones, P. J. Wiseman and J. B. Goodenough, *Mater. Res. Bull.*, **15**, 783 (1980) ; J. B. Goodenough, K. Mizushima and T. Takeda, *Jpn. J. Appl. Phys.*, **19**, 305 (1980).
2. M. G. S. R. Thomas, W. I. F. David, J. B. Goodenough and P. Groves, *Mater. Res. Bull.*, **20**, 1137 (1985).
3. J. R. Dahn, U. von Sacken and C. A. Michal, *Solid State Ionics*, **44**, 87 (1990).
4. J. R. Dahn, U. von Sacken, M. W. Juzkow and H. Al-Janaby, *J. Electrochem. Soc.*, **138**, 2207 (1991).
5. T. Ohzuku, A. Ueda and M. Nagayama, *J. Electrochem. Soc.*, **140**, 1862 (1993).
6. M. Broussely, F. Perton, J. Labat, R. J. Staniewicz and A. Romero, *J. Power Sources*, **43-44**, 209 (1993).
7. C. Delmas and I. Saadoune, *Solid State Ionics*, **53-56**, 370 (1992).
8. C. Delmas, I. Saadoune and A. Rougier, *J. Power Sources*, **43-44**, 595 (1993).
9. A. Ueda and T. Ohzuku, *J. Electrochem. Soc.*, **141**, 2010 (1994).
10. J. N. Reimers, E. Rossen, C. D. Jones and J. R. Dahn, *Solid State Ionics*, **61**, 335 (1993).
11. E. Rossen, C. D. W. Jones and J. R. Dahn, *Solid State Ionics*, **57**, 311 (1992).
12. M. E. Spahr, P. Novak, O. Haas and R. Nesper, *J. Power Sources*, **68**, 629 (1997).
13. T. Ohzuku and Y. Makimura, *Chem. Lett.*, **30**, 744 (2001).
14. T. Ohzuku, A. Ueda and M. Kouguchi, *J. Electrochem. Soc.*, **142**, 4033 (1995).
15. Q. Zhong and U. von Sacken, *J. Power Sources*, **54**, 221 (1995).
16. C. Delmas, M. Menetrier, L. Croguennec, I. Saadoune, A. Rougier, C. Pouillier, G. Prado, M. Grune and L. Fournes, *Electrochim. Acta*, **45**, 243 (1999).

17. C. Pouillierie, L. Croguennec, Ph. Biensan, P. Willmann and C. Delmas, *J. Electrochem. Soc.*, **147**, 2061 (2000).
18. C.-C. Chang, J. Y. Kim and P. N. Kumta, *J. Electrochem. Soc.*, **147**, 1722 (2000).
19. S. Madhavi, G. V. Subba Rao, B. V. R. Chowdari and S. F. Y. Li, *J. Power Sources*, **93**, 156 (2001).
20. K. K. Lee, W. S. Yoon, K. B. Kim, K. Y. Lee and S. T. Hong, *J. Power Sources*, **97-98**, 308 (2001).
21. J. S. Weaving, F. Coowar, D. A. Teagle, J. Cullen, V. Dass, P. Bindin, R. Green and W. J. Macklin, *J. Power Sources*, **97-98**, 733 (2001).
22. M. Broussely, Ph. Blanchard, Ph. Biensan, J. P. Planchat, K. Nechev and R. J. Staniewicz, *J. Power Sources*, **119-121**, 859 (2003).
23. C. Pouillierie, F. Pertont, Ph. Biensan, J. P. Peres, M. Broussely and C. Delmas, *J. Power Sources*, **96**, 293 (2001).
24. A. D'Epifanio, F. Croce, F. Ronci, V. Rossi Albertini, E. Traversa and B. Scrosati, *Chem. Mater.*, **16**, 3559 (2004).
25. J. Shim, R. Kosteki, T. Richardson, X. Song and K. A. Striebel, *J. Power Sources*, **112**, 222 (2002).
26. C. H. Chen, J. Liu, M. E. Stoll, G. Henriksen, D. R. Vissers and K. Amine, *J. Power Sources*, **128**, 278 (2004).
27. Y. Ito and Y. Ukyo, *J. Power Sources*, **146**, 39 (2005).
28. M. Broussely, Ph. Biensan, F. Bonhomme, Ph. Blanchard, S. Herreyre, K. Nechev and R. J. Staniewicz, *J. Power Sources*, **146**, 90 (2005).
29. T. Sasaki, T. Nonaka, H. Oka, C. Okuda, Y. Ito, Y. Kondo, Y. Takeuchi, Y. Ukyo, K. Tatsumi and S. Muto, *J. Electrochem. Soc.*, 156, A289 (2009).

30. S. Muto, T. Yoshida and K. Tatsumi, *Mater. Trans.*, **50**, 964 (2009).
31. S. Muto, Y. Sasano, K. Tatsumi, T. Sasaki, K. Horibuchi, Y. Takeuchi and Y. Ukyo, *J. Electrochem. Soc.*, **156**, A371 (2009).
32. S. Muto, K. Tatsumi, T. Sasaki, H. Kondo, T. Ohsuna, K. Horibuchi and Y. Takeuchi, *Electrochem. Solid-State Lett.*, **13**, A115 (2010).
33. Y. Kojima, S. Muto, K. Tatsumi, H. Oka, H. Kondo, K. Horibuchi and Y. Ukyo, *J. Power Sources*, in press (2011): doi.org/10.1016/j.jpowsour.2011.05.017..
34. H. Kondo, Y. Takeuchi, T. Sasaki, S. Kawauchi, Y. Itou, O. Hiruta, C. Okuda, M. Yonemura, T. Kamiyama and Y. Ukyo, *J. Power Sources*, **174**, 1131 (2007).
35. K. Tatsumi, Y. Sasano, S. Muto, T. Yoshida, T. Sasaki, K. Horibuchi, Y. Takeuchi and Y. Ukyo, *Phys. Rev. B*, **78**, 045108 (2008).
36. P. Blaha, K. Schwarz, G. K. H. Madsen, D. Kvasnicka and J. Luitz, WIEN2k, An Augmented Plane Wave + Local Orbitals Program for Calculating Crystal Properties (Karlheinz Schwarz, Techn. Universität Wien, Austria), 2001. ISBN 3-9501031-1-2
37. G. Kresse and J. Furthmuller, *Phys. Rev. B*, **54**, 11169 (1996).
38. F. Zhou, M. Cococcioni, C. A. Marianetti, D. Morgan, and G. Ceder, *Phys. Rev. B*, **70**, 235121 (2004).
39. H. Kurata, M. Tujimoto, T. Nemoto and S. Isoda *Proceedings of the 49th Symposium of the Japanese Society of Microscopy, Microscopy*, 2004, 39 suppl. 1 p.49.
40. F. Scholz, ed., *Electrochemical Methods*, 2nd ed., Springer, Berlin, 2010, p.159.
41. Z. Ogumi, *Electrochemistry*, **78**, 319 (2010).
42. Z. Ogumi, T. Abe, T. Fukutsuka, S. Yamate and Y. Iriyama, *J. Power Sources*, **127**, 72 (2004).
43. T. Abe, H. Fukuda, Y. Iriyama and Z. Ogumi, *J. Electrochem. Soc.*, **151**, A1120

(2004).

44. Y. Yamada, Y. Iriyama, T. Abe and Z. Ogumi, *Langmuir*, **25**, 12766 (2009).

45. K. Xu, *J. Electrochem. Soc.*, **154**, A162 (2007).

46. H. Gabrisch, R. Yazami and B. Fultz, *J. Power Sources*, **119-121**, 674 (2003).

Figure captions

Figure 1. Cell capacity changes for (a) NCA and (b) Mg-doped NCA during cycling at 70 °C.

Figure 2. Nyquist plots of (a) NCA and (b) Mg-doped NCA cathodes, before and after cycling. Data was collected at 20 °C and 3.78 V vs. Li⁺/Li using a three-electrode cell, with Li metal counter and reference electrodes. The charge-transfer resistance of cathode was separated by using an equivalent circuit, (c).

Figure 3. Temperature dependence of the charge-transfer resistance of (a) NCA and (b) Mg-doped NCA, before and after the cycling test. Activation energies were evaluated from the slopes of Arrhenius plots by the least-squares method, and are noted in the graphs.

Figure 4. Three-component STEM-EELS SI MCR analysis results of an Mg-doped NCA cathode before and after cycling at 70 °C. (a) Extracted spectral components common between the samples, before and after cycling. Spatial distribution maps of the spectral and residual components (b) before cycling and (c) after cycling.

Figure 5. Four-component STEM-EELSSI MCR analysis results of a Mg-doped NCA cathode before and after cycling at 70 °C: (a) Extracted spectral components. (b) Spatial distribution maps.

Figure 6. Annular dark-field images of the Mg-doped NCA cathode sample (a) before

and (c) after cycling. Energy filtered images showing fluorine distribution (b) before and (d) after cycling.

Figure 7. Three extracted types of O K ELNES by MCR are compared. The pre-peak positions are marked by color solid lines.

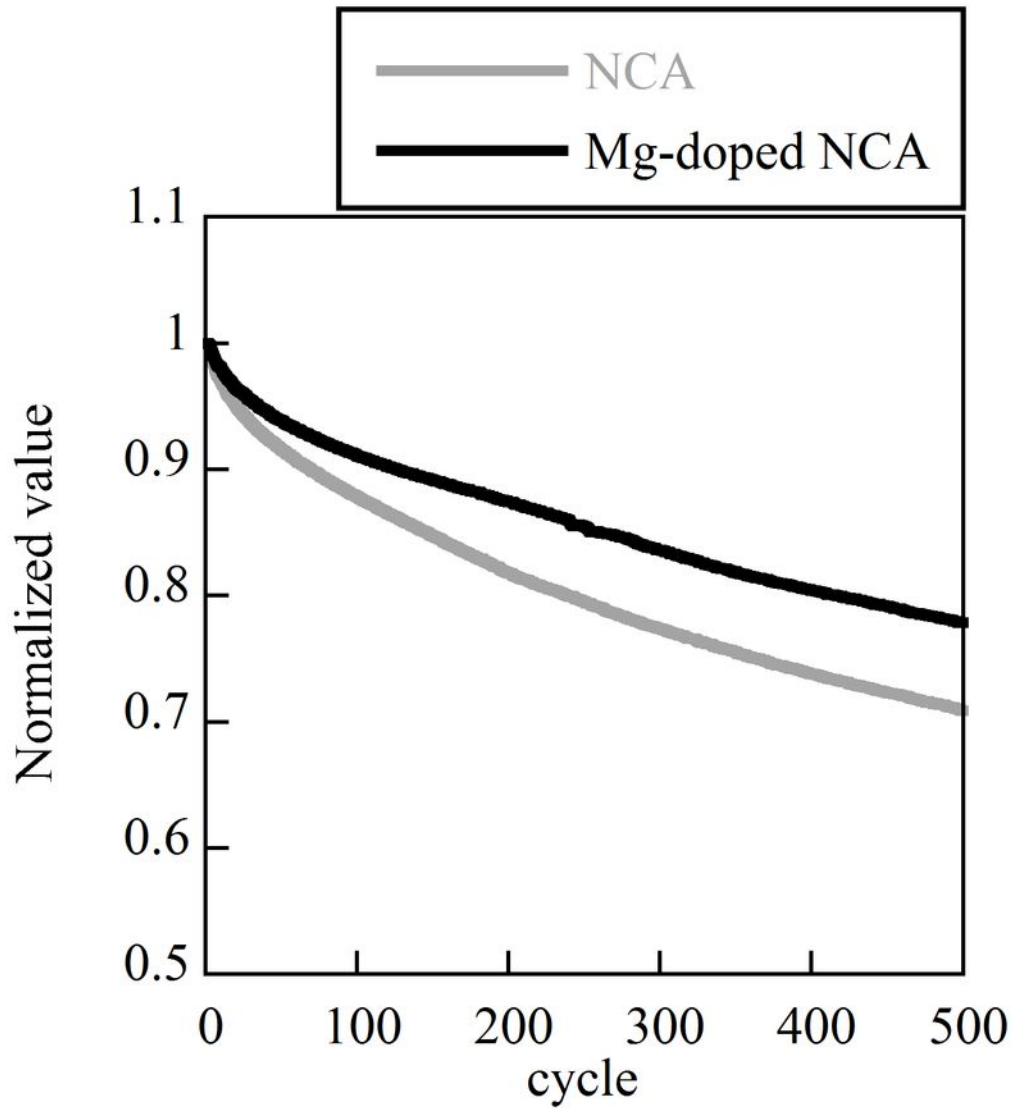
Figure 8. (a) Experimental Ni L_{2,3} ELNESs. (b) Calculated O K ELNES profiles. The pre-peak positions in the experimental spectra (Fig. 6) are inset as solid color lines.

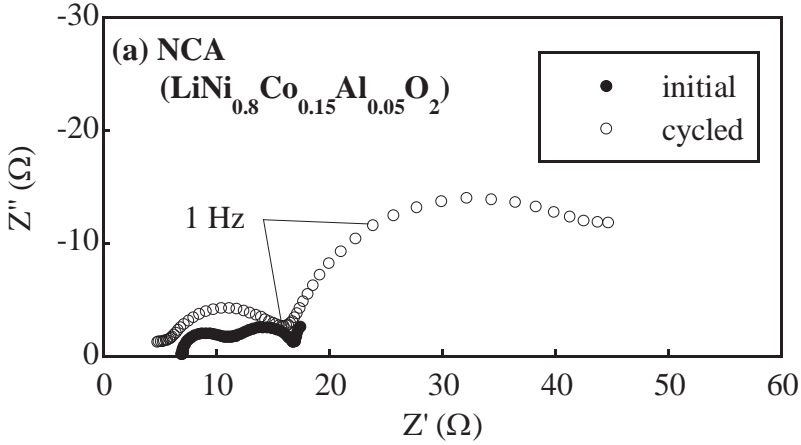
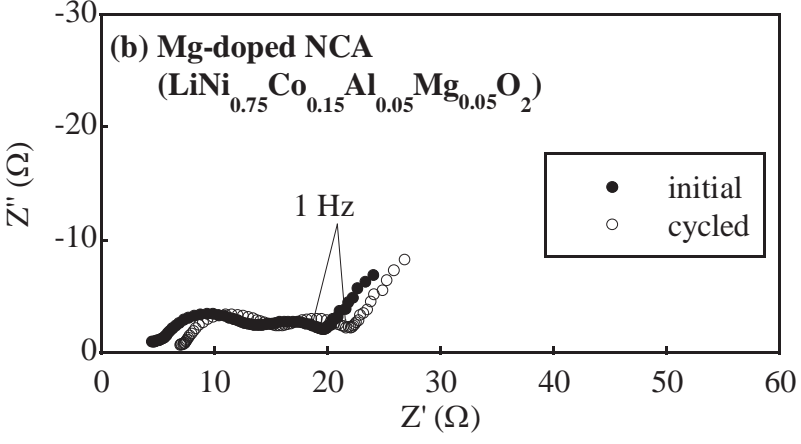
Table 1 Capacity and I-V resistance of cells using NCA and Mg-doped NCA cathodes, before and after cycling. The capacity was normalized by the weight of the cathode material contained in the cylindrical cell. I-V resistance was calculated by the response of the cell voltage over 10 s to a constant current. All the data was obtained at 20 °C.

	Capacity (mAh/g)		I-V resistance (10 s) (mΩ)	
	Fresh	Cycled	Fresh	Cycled
LiNi _{0.8} Co _{0.15} Al _{0.05} O ₂ (NCA)	169.3	132.0 (-22.0%)	51.8	79.7 (+53.9%)
LiNi _{0.75} Co _{0.15} Al _{0.05} Mg _{0.05} O ₂ (Mg-doped NCA)	147.9	125.4 (-15.2%)	53.7	69.4 (+29.2%)

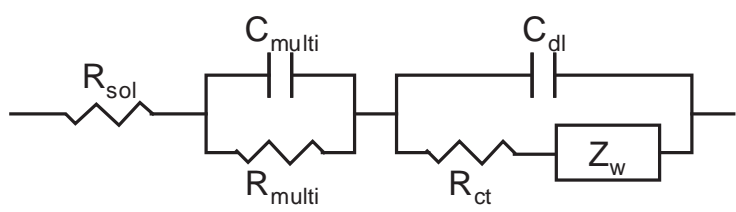
Table 2 Average particle radius, $\langle r \rangle$, average thickness, $\langle \Delta z \rangle$, standard deviation, σ , and volume fraction, $\Delta V/V$ of the product phase, roughly estimated from the experimental results for the respective samples of Mg-doped NCA.

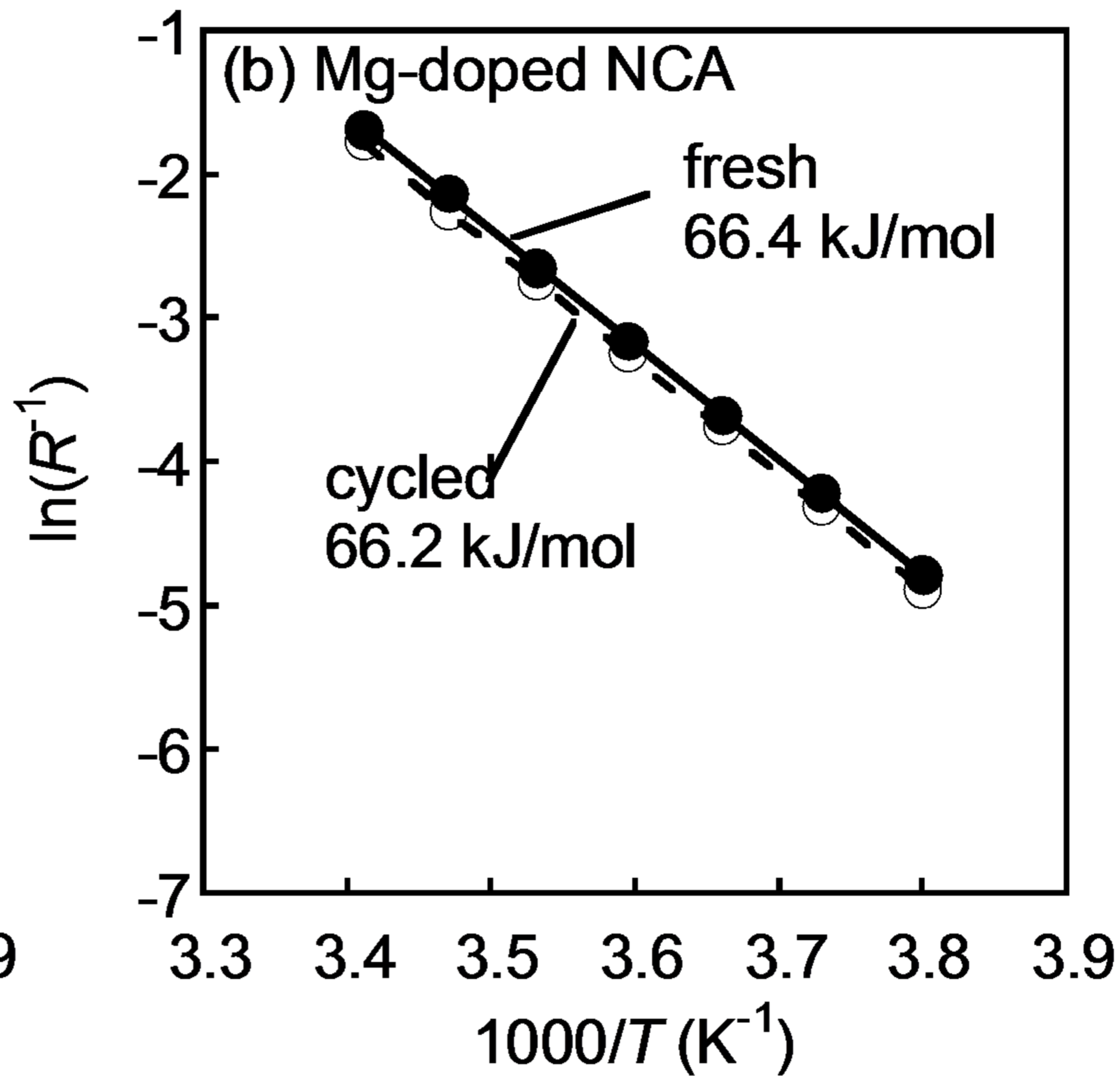
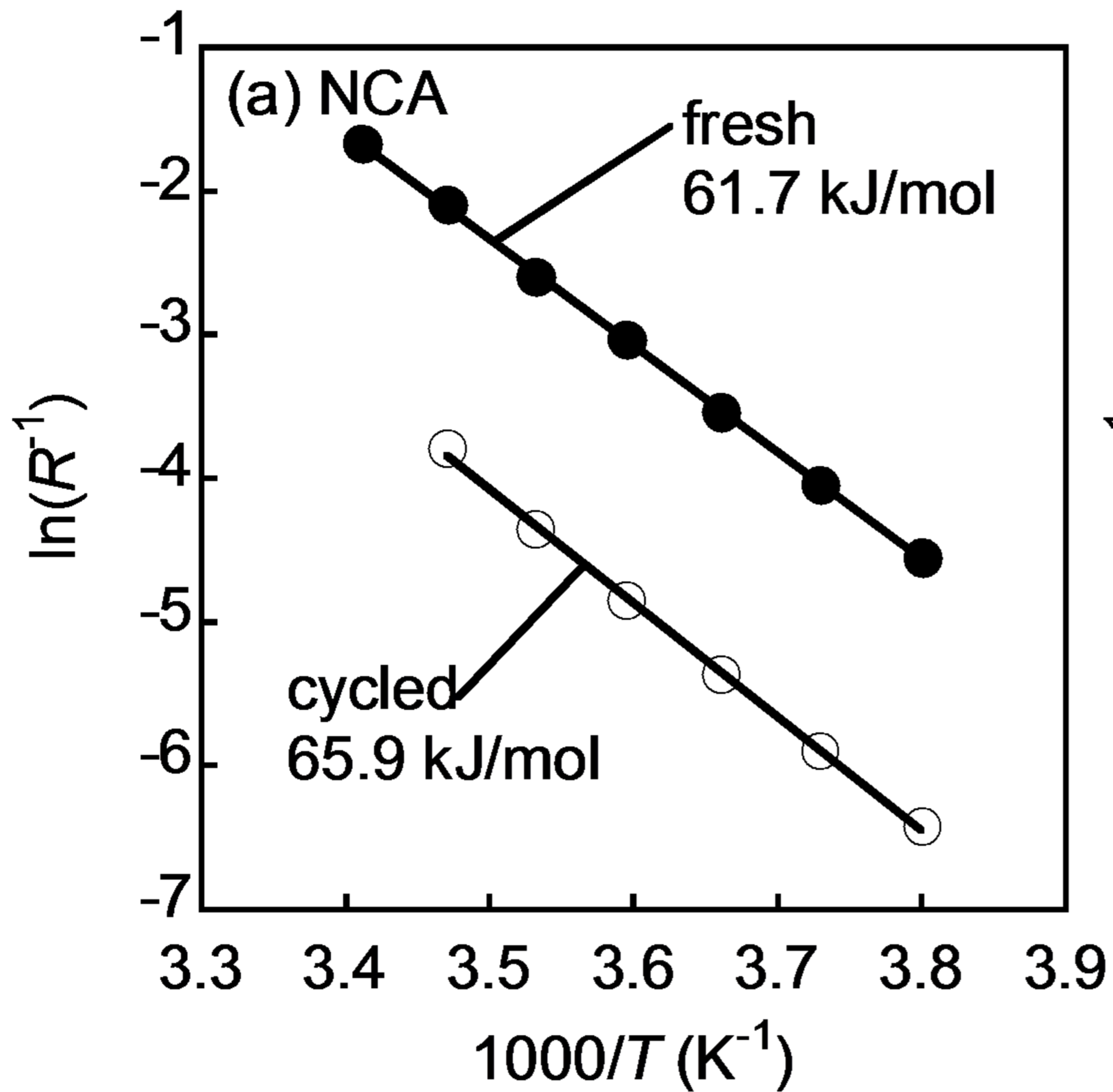
	Initial conditioning	70 °C
$\langle r \rangle$ (nm)	470	370
$\langle \Delta z \rangle$ (nm)	50	50
σ (nm)	30	20
$1-\Delta V/V$	0.69(10)	0.63(11)
$\Delta(\Delta V/V) \times 100$ (%)	-	-9(15)

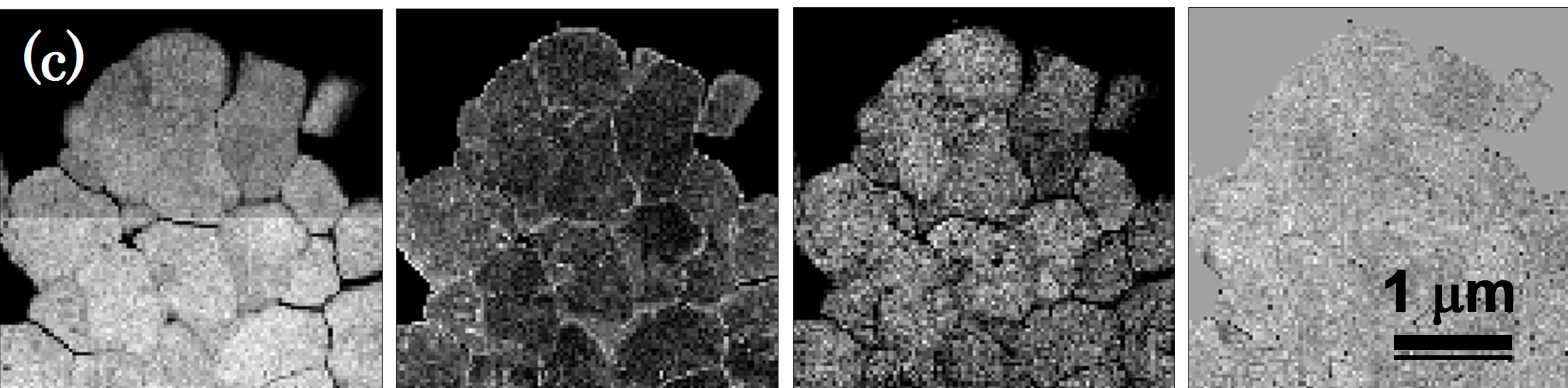
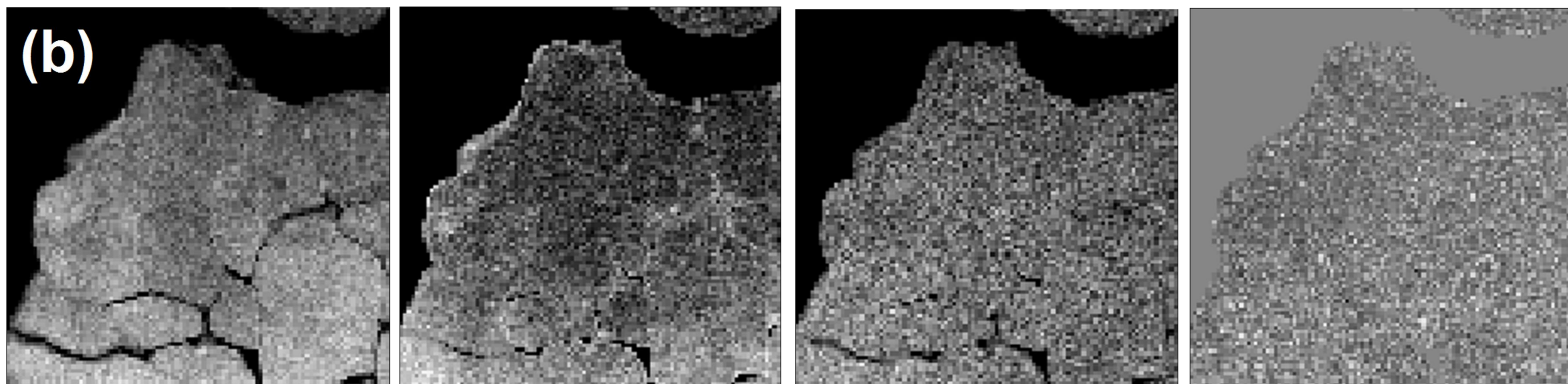
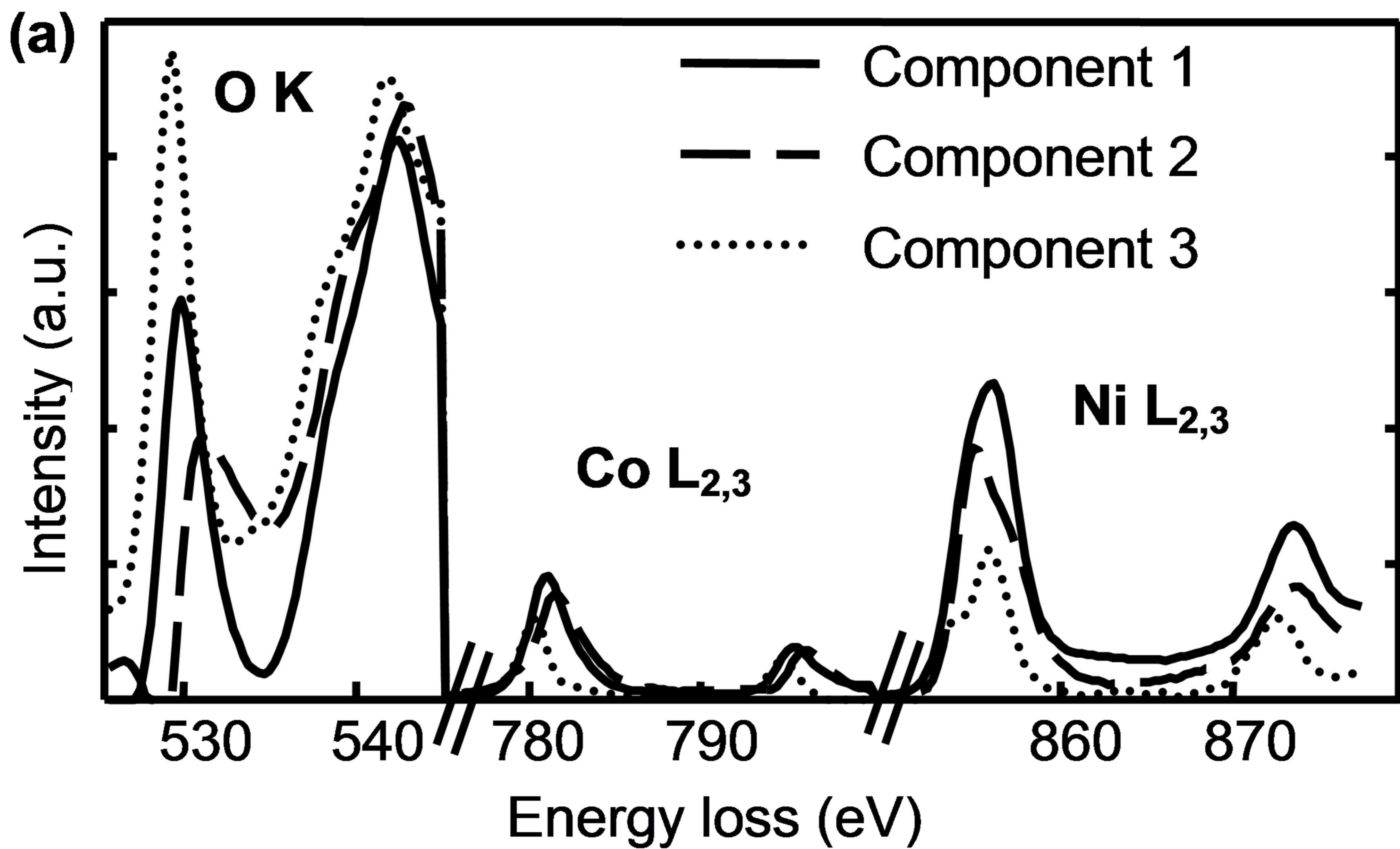




(c) Equivalent circuit







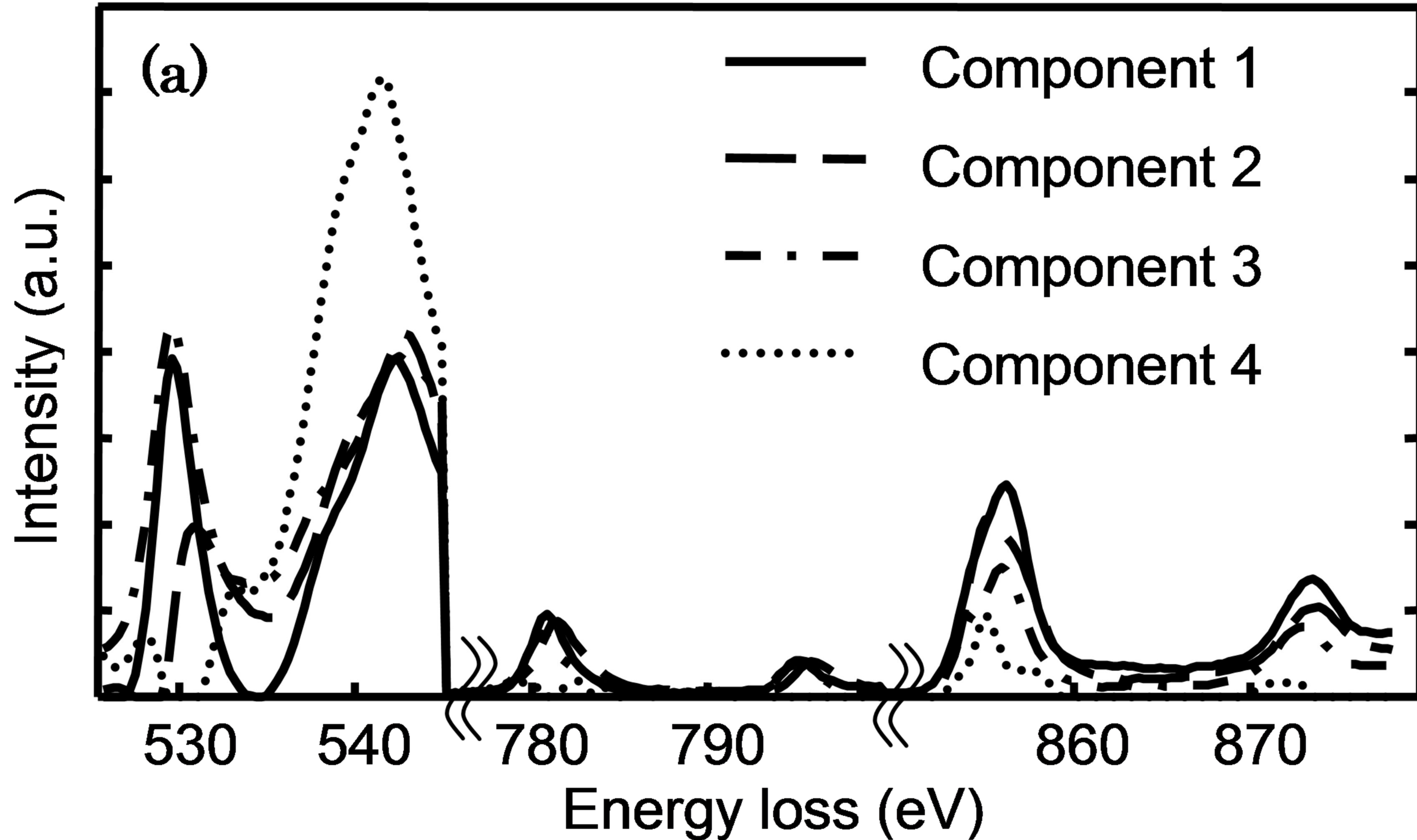
Comp.1

Comp.2

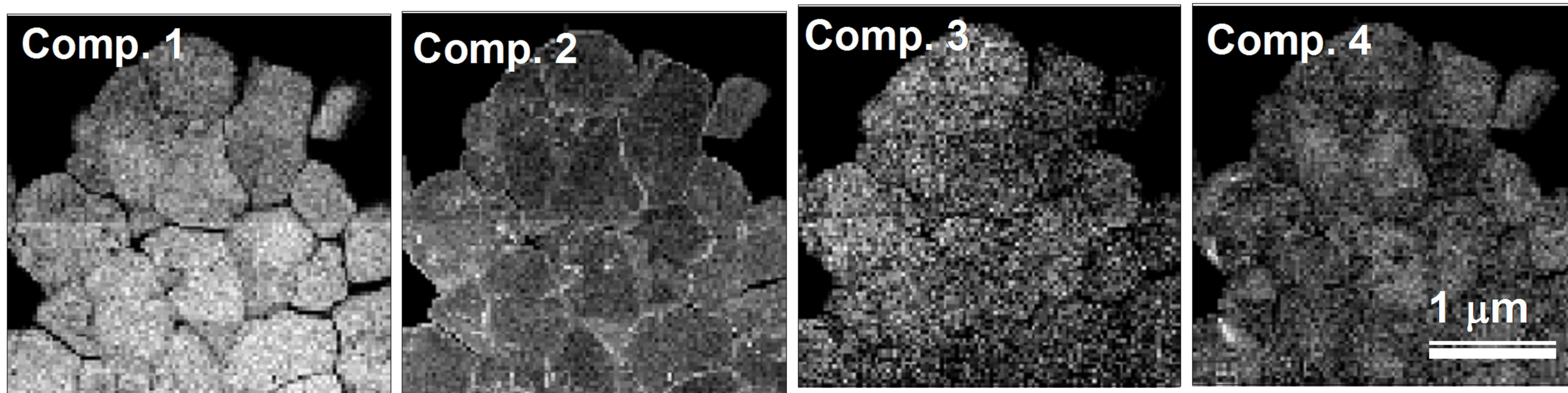
Comp.3

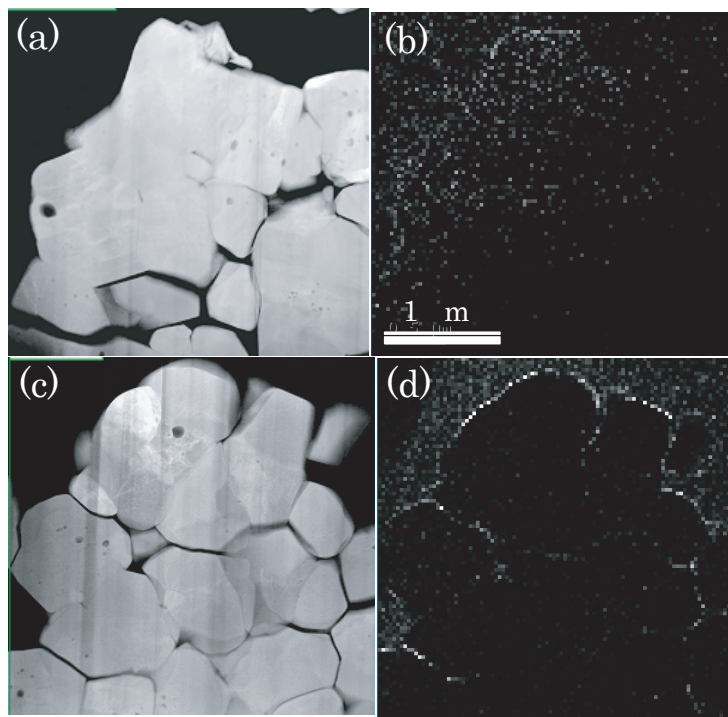
residual

1 μm



(b)





Intensity (a.u.)

